A Nonlinear Fuel Optimal Reaction Jet Control Law

Eric F. Breitfeller[*] and Lawrence C. Ng[†]

Lawrence Livermore National Laboratory

P.O. Box 808, L-278, Livermore, CA 94551

Abstract

We derive a nonlinear fuel optimal attitude control system (ACS) that drives the final state to the desired state according to a cost function that weights the final state angular error relative to the angular rate error. Control is achieved by allowing the pulse-width-modulated (PWM) commands to begin and end anywhere within a control cycle, achieving a pulse width pulse time (PWPT) control. We show through a MATLAB® Simulink model that this steady-state condition may be accomplished, in the absence of sensor noise or model uncertainties, with the theoretical minimu m number of actuator cycles. The ability to analytically achieve near-zero drift rates is particularly important in applications such as station-keeping and sensor imaging. Consideration is also given to the fact that, for relatively small sensor and model errors, the controller requires significantly fewer actuator cycles to reach the final state error than a traditional proportional- integral-derivative (PID) controller. The optimal PWPT attitude controller may be applicable for a high performance kinetic energy kill vehicle.

Introduction

In problems related to the attitude control of rigid bodies, it is often advantageous to design an attitude control system that is optimal in some way relative to a set of system constraints. Most often cited are constraints of time and fuel. A constraint pertinent to some systems regards the total number of PWM commands sent to the actuators. In our case that is represented by valve commands sent to the ACS jets. A PID controller is simple to implement (Wie [1], 1998), takes few CPU cycles, and usually is robust in most applications. Sliding mode controllers are likewise robust and easy to implement (Wertz[2], 1978). Both of these control systems share a potential common trait, in an environment where sensor noise exists, of requesting numerous PWM commands while dithering about their phase-plane trajectories. These effects can be minimized by introducing deadbands and other nonlinear elements at the expense of system response and accuracy.

We derive a single-axis PWPT ACS that minimizes the total number of valve commands while simultaneously minimizes a cost function dependent on the final state errors. We first apply the single-axis controller to a 1-DOF simulated system, and then to a 3-DOF system, where each axis is controlled by the single-axis controller. This allows us to evaluate its effectiveness in the presence of coupling through the inertia matrix. Phase-plane plots of angle versus angle rate are given as well as plots of the valve commands. Monte Carlo runs are made using Simulink in order to investigate controller sensitivities to gyro noise and camera noise. Published results (Garcia [3], 1998) are shown in work done previously in support of MicroSat pointing and control development at LLNL.

Pulse Width Modulation (PWM)

An approximation to an idealized linear command may be represented as in Figure-1, and is shown to start at the beginning of the control cycle and to end within the control cycle, or it may continue into the next cycle if the command is saturated.

Approximated PWM force

ideal linear force

$0 \quad t_{on} \quad T_{ACS}$
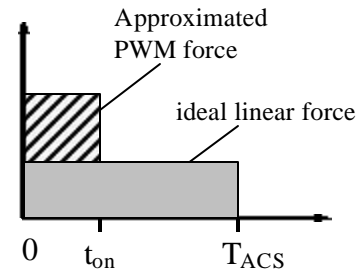
Figure-1: Ideal linear force command shown with PWM approximation

A discrete approximation to the ideal jet turn on time request can be made as follows,

$$t_{on} = \begin{cases} \dfrac{F_{cmd}}{F_{jet}} \cdot T_{ACS} & ; \ (F_{cmd} \le F_{jet}) \\ sign(F_{cmd}) \cdot T_{ACS} & ; \ (F_{cmd} > F_{jet}) \end{cases}$$

Figure-2 illustrates a single-axis PWM control loop that provides feedback on error and error rate.

Report Documentation Page

Report Date	Report Type	Dates Covered (from... to)
29JUL2002	N/A	-

Title and Subtitle	Contract Number
A Nonlinear Fuel Optimal Reaction Jet Control Law	
	Grant Number
	Program Element Number

Author(s)	Project Number
	Task Number
	Work Unit Number

Performing Organization Name(s) and Address(es)	Performing Organization Report Number
Lawrence Livermore National Laboratory P.O. Box 808, L-278 Livermore, CA 94551	

Sponsoring/Monitoring Agency Name(s) and Address(es)	Sponsor/Monitor's Acronym(s)
	Sponsor/Monitor's Report Number(s)

Distribution/Availability Statement
Approved for public release, distribution unlimited

Supplementary Notes
See Also ADM201460. Papers from Unclassified Proceedings from the 11th Annual AIAA/MDA Technology Conference held 29 July - 2 August 2002 in Monterey, CA., The original document contains color images.

Abstract

Subject Terms

Report Classification	Classification of this page
unclassified	unclassified

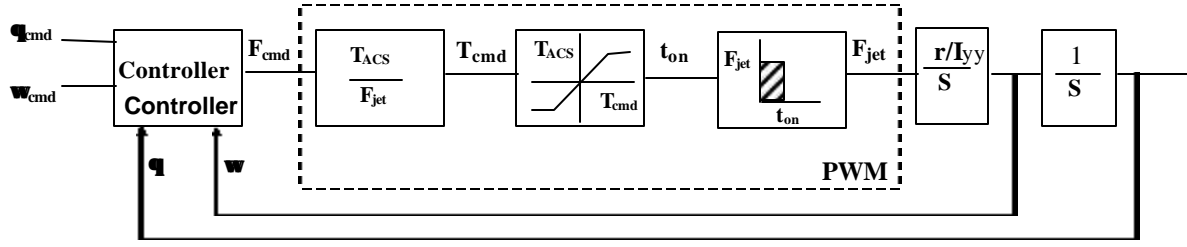| Classification of Abstract	Limitation of Abstract
unclassified	UU

Number of Pages
9

Figure-2: Simplified single-axis controller

Nonlinear Controller Derivation

A continuous single-axis system may be described by,

$$\dot{q} = w$$
$$\dot{w} = \frac{F_{jet} \cdot r}{I_{yy}} = a \qquad (1)$$

where r is the jet control moment arm, I_{yy} is the inertia term, and F_{jet} is the fixed-amplitude jet force. A discrete representation is given by,

$$q_T = q_0 + w_0 \cdot T_{ACS} - \frac{1}{2}a \cdot p^2 + a \cdot p \cdot (T_{ACS} - t_1)$$

$$w_T = w_0 + a \cdot p, \qquad (2)$$

where T_{ACS} is the control cycle period, t_1 marks the beginning of the jet pulse, and p is the pulse width, $p = t_2 - t_1$, where, t_2 marks the end of the pulse width.

Figure-3 shows the states, q and w as a function of time for a jet pulse occurring over a particular time period, t_1 to t_2. Note that the beginning of the pulse is not shown to coincide with the beginning of the control cycle, and it is this feature of both pulse width and pulse time that the nonlinear controller relies on to satisfy the two error criteria of $\Delta q \rightarrow 0, \Delta w \rightarrow 0$, where $\Delta q = q_d - q_T$, $\Delta w = w_d - w_T$ and, q_d and w_d are the desired end states.

The cost function is defined as,

$$J(t_1, p) = (q_d - q_T)^2 + k \cdot (w_d - w_T)^2 \qquad (3)$$

which, as seen from Eq.-2, allows for two degrees of freedom, t_1 and p, in order to satisfy the two criteria of $\Delta q \rightarrow 0, \Delta w \rightarrow 0$. The parameter k defines the relative weighting between the position and rate error. Note that because of the PWPT solution must lie within the next ACS control interval, a constrained optimization of Eq. (3) is needed.
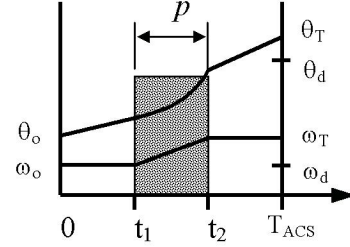

Figure-3: Discrete state transition over one ACS control cycle as a function of jet pulse width and jet pulse temporal position within the control cycle.

Referring to Figure-3, there are a total of five cases to be evaluated:

Case-1: $t_1 \geq 0$ and $t_2 \leq T_{ACS}$, where, $p = t_2 - t_1$

Case-2: $t_1 < 0$ and $t_2 \leq T_{ACS} \Rightarrow p = t_2$

Case-3: $t_1 \geq 0$ and $t_2 > T_{ACS} \Rightarrow p = T_{ACS} - t_1$

Case-4: $\dfrac{\Delta w}{a} \qquad p_{minimum\ pulse} \Rightarrow \Delta\omega \cong 0, \ t_1 = 0$

Case-5: $t_1 < 0$ and $t_2 > T_{ACS}$, large angle saturation.

The cost function of Case-1 (depicted in Figure-3) is an unconstraint case and can be evaluated against t_1 and p in order to derive expressions for their optimal values as follows,

$$\frac{\partial J}{\partial t_1} = 2 \cdot (q_d - q_T) \cdot a \cdot p \equiv 0 \Rightarrow q_d = q_T, \text{ for } p \neq 0,$$

so that,

$$\Delta q = -\frac{1}{2}a \cdot p^2 + a \cdot p \cdot (T_{ACS} - t_1)$$

$$t_1^* = T_{ACS} - (\frac{p}{2} + \frac{\Delta q}{a \cdot p}) \qquad (4)$$

We next seek the optimal value of p by taking the derivative of J w.r.t. p.

$$\frac{\partial J}{\partial p} = -2 \cdot (\boldsymbol{q}_d - \boldsymbol{q}_T) \cdot (T_{ACS} - t_1 - p)$$
$$+ k \cdot (\boldsymbol{w}_d - \boldsymbol{w}_T) \equiv 0$$

$$\Rightarrow \boldsymbol{w}_d = \boldsymbol{w}_T, \text{ since} \boldsymbol{q}_d = \boldsymbol{q}_T$$

$$\Delta \boldsymbol{w} = \boldsymbol{w}_d - \boldsymbol{w}_0 = \boldsymbol{a} \cdot p$$

$$p^* = \frac{\Delta \boldsymbol{w}}{\boldsymbol{a}} \qquad (5)$$

Case-2 implies noncausality, as it would be necessary to begin the jet pulse prior to the beginning of the current control cycle. Thus, for Case-2, the cost function is evaluated using a causal constraint by setting $t_1 = 0$,

$$\frac{\partial J}{\partial p} \equiv 0 \Rightarrow$$

$$(\boldsymbol{q}_d - \boldsymbol{q}_T) \cdot (T_{ACS} - p) - k \cdot (\boldsymbol{w}_d - \boldsymbol{w}_T) \equiv 0,$$

which leads to,

$$p^3 - 3 \cdot T_{ACS} \cdot p^2$$
$$+ 2 \cdot \left(T_{ACS}^2 + k - \frac{\Delta \boldsymbol{q}}{\boldsymbol{a}} \right) \cdot p$$
$$- \frac{2}{\boldsymbol{a}} \cdot (\Delta \boldsymbol{q} \cdot T_{ACS} + k \cdot \Delta \boldsymbol{w}) = 0 \qquad (6)$$

Eq.-6 shows that it is necessary to solve a cubic polynomial; this will also be true of Cases-3 and –4.

Case-3 corresponds to a jet pulse that is requested to turn on during the current ACS period, yet extend beyond the period. A constraint is imposed by truncating the desired pulse so that it does not extend into the next control cycle (i.e., $t_2 = T_{ACS} \Rightarrow p = T_{ACS} - t_1$). Therefore in Case-3, t_1 and p are linearly dependent on one another, allowing one degree of freedom in which to evaluate the cost function,

$$\frac{\partial J}{\partial p} \equiv 0 \Rightarrow p^3 + 2 \cdot \left(\frac{k \cdot \boldsymbol{a} - \Delta \boldsymbol{q}}{\boldsymbol{a}} \right) \cdot p$$
$$- 2 \cdot \frac{k \cdot \Delta \boldsymbol{w}}{\boldsymbol{a}} = 0 \qquad (7)$$

Case-4 pertains to the condition of entering a control cycle with an angular rate error that would produce a pulse width request that is less than the minimum impulse bit of the jet. For practical purposes this implies that $p = 0$, and by extension, $\Delta \omega \cong 0$. For Case-4 a choice is made to begin the valve command at the beginning of the control cycle, $t_1 = 0$, which leads to the following equation for determining p^*,

$$\frac{\partial J}{\partial p} \equiv 0 \Rightarrow p^3 - 3 \cdot T_{ACS} \cdot p^2 + 2 \cdot \left(T_{ACS}^2 + k - \frac{\Delta \boldsymbol{q}}{\boldsymbol{a}} \right) \cdot p$$
$$- \frac{2}{\boldsymbol{a}} \cdot \Delta \boldsymbol{q} \cdot T_{ACS} = 0 \qquad (8)$$

Case-5 is the "large-angle" or saturated case in which a solution to the previous four "small-angle" solutions does not exist. Case-5 therefore merely serves to bring the system into any of Case-1 through Case-4, the cases of our interest. Thereafter, an undisturbed system will remain captured in Cases-1,-2,-3, or -4.

Solutions to the cubic equations are computed and those that are positive and real are used in the evaluation of the cost function. The root yielding the minimum-valued cost function is denoted as p^*.

It should finally be noted that a default "Case-0" exists wherein $p^* < p_{minimum\,pulse}$ (i.e., the system state has reached equilibrium).

Figure-4 below illustrates the controller Cases, with the single-pulse switching line indicated by arrows (the axes have been normalized such that $\boldsymbol{q}_{Max} = \boldsymbol{w}_{Max}$, over ΔT_{ACS}). Case-1 includes the area in phase-space that can be reached during the current control cycle. Case-2 corresponds to the need to have pulsed prior to the current control cycle and then extend into the current. Case-3 corresponds to the need to first coast, then use a single pulse that extends beyond the current control cycle into the next. Case-4 represents $\Delta \omega \cong 0$, and Case-5 represents the large-angle region.
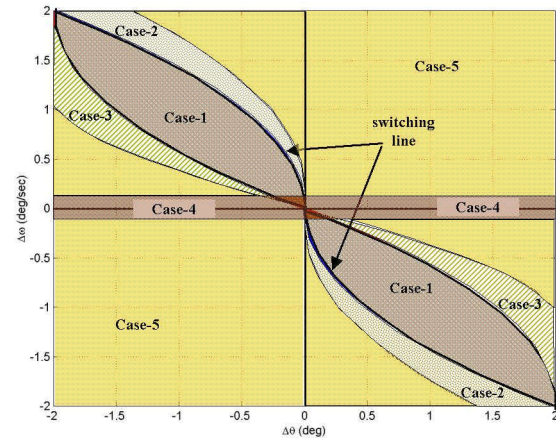

Figure-4: Controller cases shown in phase-space

Single-Axis Simulation Results

The single-axis controller is applied in a deterministic setting (noiseless sensors, ideal actuator), and then the controller is applied in a stochastic setting in order to evaluate the controller's sensitivities to gyro and camera noise.

Deterministic Scenario

A 1-DOF Simulink model was developed to evaluate the performance of the single-axis controller. An integration routine with fixed step size of $\Delta T = \frac{1}{2}$ *ms* was used and the simulations were run for 10 seconds. Other parameters included a minimum valve command of $\frac{1}{2}$ *ms*, pitch angular acceleration $\boldsymbol{a} = 0.18$ *rad/s^2*, control cycle $T_{ACS} = 25$ *ms*, and cost function weighting factor $k = 2.5$ *s^2*. A nonzero initial angle and angle rate was applied to the system which was required to drive the final states $[\theta_f \ \omega_f]^T$ to $[0 \ 0]^T$. Figure-5 shows the jet valve commands and Figure-6 shows the corresponding closeup of the valve commands for the system once it has been captured in the small-angle mode. Figure-7 illustrates the case transitions for the system in the small angle mode, Figure-8 shows the angle and angular rate errors, and the phase plane response is shown in Figure-9.
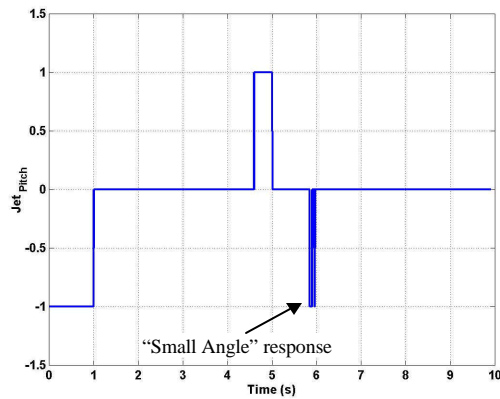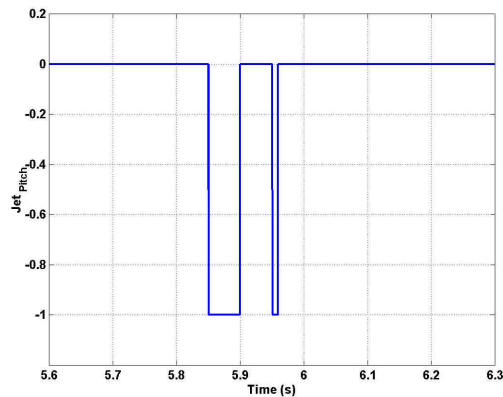

Figure-5: Jet valve commands for single-axis model

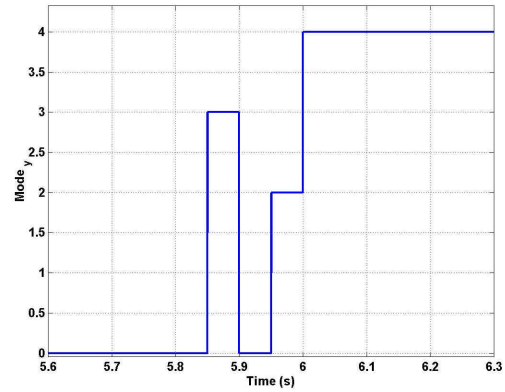**Figure-6: Closeup of Figure-5 ("Small Angle") on/off commands corresponding to Cases-1,2,3,4**

Figure-7: Closeup of case transitions for the "Small Angle" modes of Figure-5
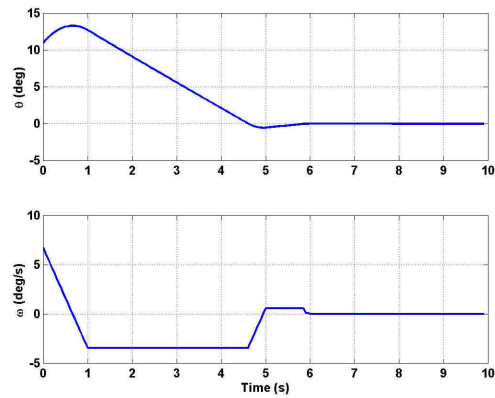

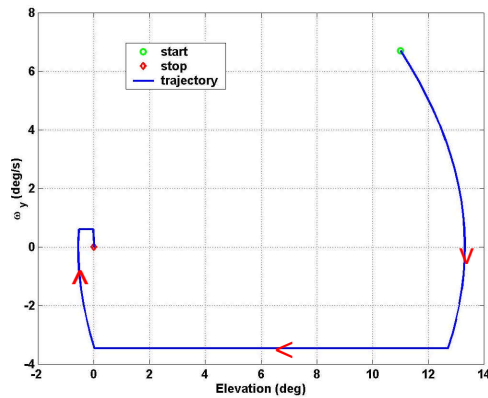**Figure-8: System state errors**

Figure-9: Phase-plane response of system

Stochastic Scenario

In order to evaluate the controller in less than ideal conditions (e.g., model sensor noises) Monte Carlo runs (N=100) were made with respect to gyro (rate) noise and camera (angle) noise, and the results

are compared against the baseline scenario. The gyro noise was chosen as a zero-mean normal distribution, with standard deviations of either 50 $\mu rad/s$ (baseline), 100 $\mu rad/s$, or 200 $\mu rad/s$, and the camera noise was chosen as a zero-mean normal distribution with standard deviations of either 100 μrad (baseline), 200 μrad, or 300 μrad. Random draws were made on the initial states $[\theta_o \ \omega_o]^T$ of each run such that $\theta_o = N(0rad, (100mrad)^2)$ and $\omega_o = N(0rad/s, (50mrad/s)^2)$, where $N(\mu, \sigma^2)$ represents a normal distribution with mean μ and standard deviation σ. The controller variables-of-interest are the final state errors ($[\Delta\theta_f \ \Delta\omega_f]^T$) and the total number of pulse commands ($p_{MEDIAN}, p_{MAXIMUM}$). Figure-9 shows the gyro sensitivity curves and Figure-10 shows the camera sensitivity curves (all results are summarized in Table-1: Summary of Monte Carlo sensitivity studies).

From Figure-10 it is seen that the variations of the final angle error, due to gyro noise, decreased from a baseline value of 0.07 *mrad* to 0.04 *mrad* at maximum gyro noise due to the increased number of pulses (dithering due to increased noise). The angle rate error increased from a baseline value of 0.04 *mrad/s* to 0.32 *mrad/sec* at maximum gyro noise. The median and maximum number of pulses increased linearly where p_{MEDIAN} varied from a baseline value of 8 *pulses* at 50 $\mu rad/s$ to 98 *pulses* at 200 $\mu rad/s$, and $p_{MAXIMUM}$ varied from 29 *pulses* to 152 *pulses*.

Looking at the variations due to camera noise, Figure-11 shows that the angle error is roughly flat with respect to camera noise, whereas the rate error significantly increases with camera noise. Both p_{MEDIAN} and $p_{MAXIMUM}$ fit well to a quadratic curve where p_{MEDIAN} increased from a baseline value of 8 *pulses* at 100 μrad to 68 *pulses* at 300 μrad, and $p_{MAXIMUM}$ increased from 29 *pulses* to 88 *pulses*.

Conclusions for the 1-DOF simulation can be summarized as follows: Assuming a noise-free environment and assuming that the controller is operating in the small-angle region (Cases-1 through –4) it has been shown that the controller can take the system from an initial state to a final state in two or three pulses, depending on the initial point in angle-angle rate phase space. In an environment with noise present, the controller is least sensitive with respcet to the final angle error, and exhibits considerable sensitivities with respect to the final angle rate error and the number of pulses required.
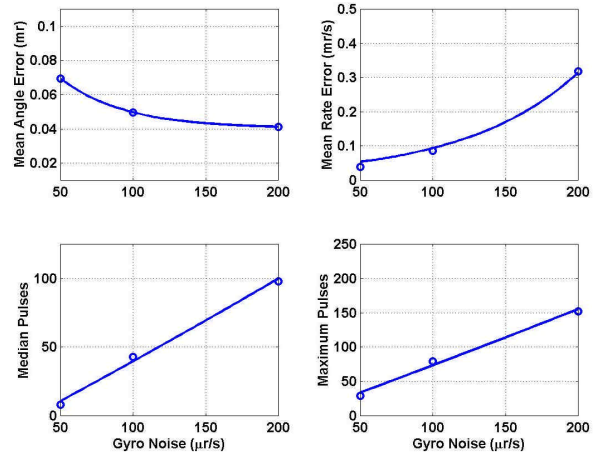

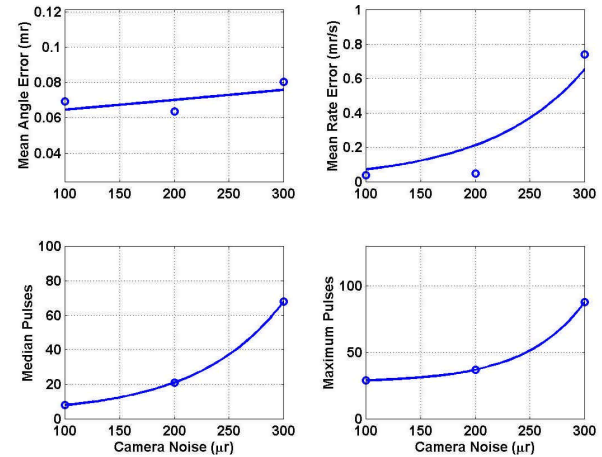**Figure-10: Monte Carlo 1-DOF sensitivities to gyro noise**

Figure-11: Monte Carlo 1-DOF sensitivities to camera noise

Three-Axis Monte Carlo Simulation Results

A fully-coupled 3-DOF Simulink model was developed in order to evaluate the performance of the single-axis controller when applied to each of the three axes independently. Eq.-9 represents the dynamics and illustrates the cross-coupling effects that occur among axes. The inertia matrix was chosen to contain only moment-of-inertia terms, and six actuator jets were modeled as opposing pairs per axis. Other parameters remained the same as in the 1-DOF simulation (e.g., minimum valve commands of 1.0 *ms*). The pitch angular acceleration, $a_{pitch} = 0.18 \ rad/s^2$, remained the same, and roll and yaw

angular accelerations were arbitrarily chosen as, $\boldsymbol{a}_{roll}$ = 0.22 *rad/s²* and $\boldsymbol{a}_{yaw}$ = 0.20 *rad/s²*.

$$\dot{\vec{Q}} = -\frac{1}{2}[\Omega] \cdot \vec{Q}$$

$$\dot{\vec{w}} = I^{-1} \cdot (\vec{t} - \vec{w} \times (I \cdot \vec{w})) \tag{9}$$

where, $\vec{Q}$ is the attitude quaternion defined as $\vec{Q} = [q_{scalar} \quad \vec{q}_{vector}]$, $[\Omega]$ is a skew symmetric matrix comprised of elements of the angular rate vector, $\vec{w}$, I is the inertia matrix and, $\vec{t}$ is the applied jet torques.

As in the 1-DOF scenario, Monte Carlo runs (N=100) were made with respect to gyro noise and camera noise, and the results are compared against the baseline scenario. The gyro noise was chosen as zero-mean Gaussian, with standard deviations of either 50 $\boldsymbol{m}$*rad/s* (baseline), 100 $\boldsymbol{m}$*rad/s*, or 200 $\boldsymbol{m}$*rad/s* and the camera noise was also chosen as zero-mean Gaussian with standard deviations of either 100 $\boldsymbol{m}$*rad* (baseline), 200 $\boldsymbol{m}$*rad*, or 300 $\boldsymbol{m}$*rad*. Random draws were made on the initial states $[\theta_0 \quad \omega_0]^T$ of each run such that $\theta_0 = N(0rad, (100mrad)^2)$ and $\omega_0 = N(0rad/s, (50mrad/s)^2)$, and the controller was required to drive the angles and angular rates to zero.

Figures-12 and -13 show the cumulative sensitivity results for gyro noise and camera noise, respectively. In this context, "cumulative", with respect to the angle errors and angular rate errors, is defined by the norm of the three-axis errors, whereas cumulative with respect to the number of pulses is defined by the sum of the three-axis pulses. The cumulative 3-DOF p_{MEDIAN} for the baseline scenario is 19*pulses* which, when compared to the 1-DOF system's baseline scenario of 8*pulses*, is slightly less than an ideal increase of a factor-of-three. Thus, it could be speculated that the coupling among axes is assumed to be responsible for the unexpected five fewer pulses in the 3-DOF system. Similarly, the cumulative 3-DOF $p_{MAXIMUM}$ for the baseline scenario is 63*pulses* which, when compared to the 1-DOF system's baseline scenario of 29*pulses*, is again below the ideal increase of a factor-of-three. A similarly consistent pattern holds for the 3-DOF angle and angular rate errors as in the 1-DOF system.
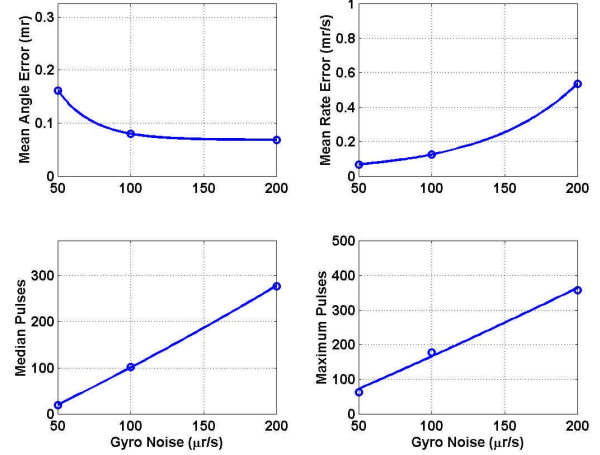

Figure-12: Monte Carlo 3-DOF cumulative sensitivities to gyro noise

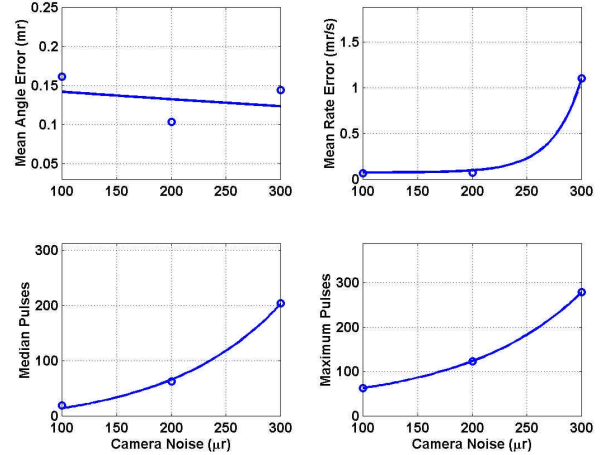**Figure-13: Monte Carlo 3-DOF cumulative sensitivities to camera noise**

In the 3-DOF system the angle errors and angular rate errors are roughly larger by a factor of $\sqrt{3}$ as compared to those in the 1-DOF system. Table-1 summarizes the results of the 1- and 3-DOF sensitivity studies for the nonlinear controller as well as results for a conventional PID controller (PID results are shown in parentheses). Similar higher-

Parameter	Variable	1-DOF Baseline σ_{Gyro}=50µrad/sec σ_{Camera}=100µrad	1-DOF Max σ_{Gyro} σ_{Gyro}=200µrad/sec σ_{Camera}=100µrad	3-DOF Baseline σ_{Gyro}=50µrad/sec σ_{Camera}=100µrad	3-DOF Max σ_{Gyro} σ_{Gyro}=200µrad/sec σ_{Camera}=100µrad
Gyro	$\Delta\theta_{Final}$ (*mrad*)	0.07 (0.29[*])	0.04 (0.18)	0.16 (1.42)	0.07 (1.05)
Gyro	$\Delta\omega_{Final}$ (*mrad/s*)	0.04 (0.09)	*0.32 (0.06)*	0.07 (0.14)	*0.54 (0.15)*
Gyro	p_{MEDIAN} (*pulses*)	8 (32)	*98 (28)*	19 (100)	*277 (108)*
Gyro	$p_{MAXIMUM}$ (*pulses*)	29 (51)	*152 (40)*	63 (126)	*358 (136)*

Parameter	Variable	1-DOF Baseline σ_{Gyro}=50µrad/sec σ_{Camera}=100µrad	1-DOF Max σ_{Camera} σ_{Gyro}=50µrad/sec σ_{Camera}=300µrad	3-DOF Baseline σ_{Gyro}=50µrad/sec σ_{Camera}=100µrad	3-DOF Max σ_{Camera} σ_{Gyro}=50µrad/sec σ_{Camera}=300µrad
Camera	$\Delta\theta_{Final}$ (*mrad*)	0.07 (0.29)	0.08 (0.14)	0.16 (1.42)	0.14 (1.20)
Camera	$\Delta\omega_{Final}$ (*mrad/s*)	0.04 (0.09)	*0.74 (0.05)*	0.07 (0.14)	*1.10 (0.14)*
Camera	p_{MEDIAN} (*pulses*)	8 (32)	*68 (25)*	19 (100)	*204 (113)*
Camera	$p_{MAXIMUM}$ (*pulses*)	29 (44)	*88 (57)*	63 (126)	*278 (146)*

Table-1-a,b: Summary of nonlinear controller Monte Carlo sensitivity studies ([*]PID controller results shown in parentheses)

level patterns are seen in the 3-DOF and 1-DOF simulations, e.g., final angle errors decrease with increasing gyro noise due to dithering, angular rate errors increase quadratically for gyro and camera noise, median and maximum pulses are linear with respect to gyro noise and quadratic with respect to camera noise.

Comparison of the Nonlinear and PID Controllers

Several observations can be extracted from Table-1 regarding the relative performance of the nonlinear controller with a conventional PID controller (used in this paper as a benchmark for comparison purposes). The first observation is that the nonlinear controller performs better, with low noise sensors (baseline scenario), than the PID controller for all four metrics considered ($\Delta\theta_{Final}$, $\Delta\omega_{Final}$, p_{MEDIAN}, $p_{MAXIMUM}$). Therefore, for low noise applications (e.g., gyro noise = 50 *mrad/s*, and camera noise = 100 *mrad*), the nonlinear controller provides better state control with fewer pulses. This is expected since the nonlinear controller solves for precise solutions required to remove state errors. However, at higher sensor noise levels (e.g., gyro

noise = 200 *mrad/s*, and camera noise = 300 *mrad*), only the final angular state error, $\Delta\theta_{Final}$, is smaller for the nonlinear controller. Conversely, when regarding the final angular rate error, $\Delta\omega_{Final}$, and number of median and maximum actuator pulse commands, the PID controller shows superior performance in the high noise scenario (shown in *italics* in Tables1-a,-b).

Summary, Conclusions, and Recommendations

It has been demonstrated that the optimal single-axis nonlinear controller, when applied to a noise-free 1-DOF model, eliminates the initial state errors to within the tolerance of the minimum pulse width of the jets and the nonideality introduced by two constraints in the controller's derivation. The first constraint occurred in Case-2, where the cost function was evaluated by setting t_1=0 (which led to Eq.-6). The second constraint occurred in Case-4, where the minimum impulse of the jet forced us to solve the cubic equation by using $\Delta\omega \cong 0$ (which led to Eq.-8). Irrespective of errors introduced by these variations on the ideal solution, the controller was

shown to require either two or three pulses to correct for initial errors, depending upon the initial phase-plane state.

Monte Carlo runs were made using a 1-DOF model in order to observe the sensitivity of the controller to gyro and camera noise, from which it was concluded that final angle errors decrease with increasing gyro noise due to dithering and angular rate errors increase quadratically for gyro and camera noise. The median and maximum pulses increase linearly with respect to gyro noise, and increase quadratically with respect to camera noise.

Monte Carlo runs were also made using a 3-DOF model in order to observe the sensitivity of the controller to gyro and camera noise, and to additionally observe how well the controller performed in the presence of a fully-coupled three-axis model. It was observed that the coupling among axes did not significantly change the characteristics of the controller's response, i.e., it behaved similarly as in the 1-DOF model with a linear scaling effect created by the fact that there were now three axes.

A comparison between the nonlinear controller and a conventional PID controller was made. It was concluded that the nonlinear controller performed better in a lower noise environment with respect to all four performance metrics, and also in the higher noise environment with respect to the final angular error. However, the PID controller performed better in a higher noise environment on three of the four metrics (final angular rate error, and median and maximum number of pulses). The Monte Carlo simulations have demonstrated the usefulness of the nonlinear controller in an application where the sensor (and by extension the actuator) noise characteristics are below some overall system-level-dependent threshold. An example of this kind of application is the requirement for precision pointing and station-keeping of an exo-atmospheric satellite.

One explanation for the seemingly poor performance of the PWPT controller, at very high angle and angular rate sensor noise, can be attributed to the fact that the cost function weighting factor, k, did not capture the full relationship between the sensor noise characteristics (i.e., sensor covariance matrix, R). The cost function could have been reformulated as,

$$J = \left[\begin{pmatrix} \boldsymbol{q}_d - \boldsymbol{q}_T \end{pmatrix} \quad \begin{pmatrix} \boldsymbol{w}_d - \boldsymbol{w}_T \end{pmatrix}\right] \cdot R^{-1} \cdot \left[\begin{pmatrix} \boldsymbol{q}_t - \boldsymbol{q}_T \end{pmatrix} \quad \begin{pmatrix} \boldsymbol{w}_d - \boldsymbol{w}_T \end{pmatrix}\right]^{\mathsf{T}}$$

$$\text{where,} \quad R = \begin{bmatrix} \boldsymbol{s}^2 qq & \boldsymbol{s}^2 qw \\ \boldsymbol{s}^2 qw & \boldsymbol{s}^2 ww \end{bmatrix}.$$

We believe with the above new formulation of the cost function, the performance of the PWPT controller will be improved significantly.

It should be noted that this controller was derived to satisfy the requirement of taking the system from an initial to a final point on the phase plane. Thus, the controller does not explicitly address the issue of tracking a moving target. However, a predictive filter could be implemented that supplies the controller with nonstationary endpoints at each control cycle, thereby allowing the controller to track a moving target. Further studies should be conducted to quantify, for this more general scenario (i.e., a moving target), the performance of the single-axis controller relative to a conventional controller (e.g., PID, sliding mode).

Controller stability as a function of the weighting parameter, k (as shown in Eq.-3) should also be studied. We have not derived a Lyapanov-type stability proof. However, by inspection of Eq.-3 it is observed that the controller's damping is directly related to the weighting parameter, k, and that as $k \to 0$ the system becomes marginally stable.

References

[1] Wertz, James R., <u>Spacecraft Attitude Determination and Control</u>, Kluwer Academic Publishers, 1978.

[2] Wie, Bong, <u>Space Vehicle Dynamics and Control</u>, AIAA Education Series, 1998.

[3] Garcia, Fermin, "A Non-linear Fuel Optimal Control Law for Spacecraft Attitude Control with Reaction Jets," MIT M.S. Thesis, 1998.

Biography

Dr. Lawrence C. Ng received his B.S. and M.S. degrees in Aeronautics and Astronautics from the Massachusetts Institute of Technology in early 1970s, and a Ph.D. degree in Electrical Engineering and Computer Sciences from the University of Connecticut in 1983 under a Naval Undersea Warfare Center (NUWC) Fellowship. In addition, Dr. Ng received his commission as an Air Force officer in 1973 and served at the Hanscom Air Force Base in Bedford, MA. His work experience includes: four years with General Dynamics Electric Boat Division in Groton, CT, responsible for the development of the TRIDENT submarine digital control systems; seven years at the NUWC where he led the development of the advanced sonar signal processing for the Seawolf submarine. Since 1986, he joined the Lawrence Livermore National Laboratory where he was the group leader of the signal/image processing and control group and is currently the Chief Scientist for the Advanced Interceptor Technology Program. Dr. Ng is focusing his research in micro-spacecraft guidance and control, integrated ground testing, and ballistic missile defense systems analysis. In addition Dr. Ng is a member of several professional societies, including honorary memberships in Sigma Xi, Tau Beta Pi, and the National Research Council. He has published numerous papers in signal estimation and precision vehicle guidance and control.

Eric F. Breitfeller has been an electrical engineer at Lawrence Livermore National Laboratory (LLNL) from 1989-1996 and 1997-present. From 1996-1997 he was at Hughes Missile Systems Company. He received his M.S.E.E. in 1988, from Ohio State University, with emphasis on control systems. From 1990-1992 he worked on guidance, navigation, and control (GNC) 6DOF simulations related to the Brilliant Pebbles program. Subsequently, he supported BMDO through the POET, where he developed a 6DOF simulation that was used in trade studies as they related to missile intercept scenarios. While at Hughes (Raytheon) he developed the attitude control system (ACS) for the Exo-atmospheric Kill Vehicle (EKV). Upon returning to LLNL in 1997 he assumed the lead GNC engineering position on the former Clementine-II program (currently the MicroSat Technology program). Precision control and estimation algorithms were designed in a 6DOF environment, and then applied to the fully-functional 5DOF (3DOF ACS + 2DOF translation) hot-gas micro-satellite. While not working on missile intercept problems, he has been involved in robotic applications related to the alignment of optical fibers to wave guides, and to beam steering of single-beam linear particle accelerators.